Proceedings of the 3rd International Conference on Machine Learning and Automation
DOI: 10.54254/2755-2721/2025.29116

Three-Phase Vienna Rectifier Current Decoupling Control in LADRC with DDC-LESO

Yuhan Guo[1], Guoji Liu[1], Yibo Guo[2], Xiaolei Che[1*]

[1]*College of Physics, Jilin University, Changchun, China*
[2]*College of Energy and Electrical Engineering, Hunan Institute of Science and Technology, Yueyang, China*
**Corresponding Author. Email: yhguo23@mails.jlu.edu.cn*

Abstract. The three-phase Vienna rectifier (TP Vienna rectifier) exhibits unique advantages: unidirectional energy transmission, minimal switching devices, and immunity to bridge-arm shoot-through, rendering it an optimal AC/DC rectification solution for DC charging systems. In its vector control, transformation to the d-q axis is adopted to simplify system analysis and control; however, inherent cross-coupling between d-q axis currents, if uncompensated, degrades control performance. Conventional decoupling methods rely on accurate inductor parameters, with dynamic decoupling efficacy deteriorating significantly under parameter mismatches. To address this, this study proposes a current decoupling control strategy based on LADRC enhanced by Disturbance Differential Compensation Linear Extended State Observer (DDC-LESO). Its core lies in replacing the traditional T-LESO in LADRC with a DDC-LESO, which incorporates an additional state variable atop T-LESO to strengthen total disturbance observability. This innovation enables DDC-LESO to observe and compensate for coupling-induced disturbances, achieving complete decoupling even under inductance parameter mismatches. Comparative analyses under varying inductance parameters validate that the proposed DDC-LESO-enhanced LADRC-based decoupling control exhibits superior robustness against inductance variations, thus confirming the methodology's feasibility.

Keywords: Three-phase Vienna Rectifier, decoupling control, ADRC, perturbation differential compensated linear expanded state observer

1. Introduction

The TP Vienna rectifier features superior performance, a streamlined topology, and a maximum reverse voltage across power switching devices equivalent to half the bus voltage. Compared with three-level rectifier topologies, it eliminates the need for dead-time setting and employs fewer power switching devices, thus garnering extensive attention and in-depth research from scholars domestically and internationally. This renders it an optimal solution for AC/DC rectification in DC charging systems [1,2].

In the vector control workflow of the TP Vienna rectifier, the real-time phase angle θ of the grid voltage is acquired via a phase-locked loop (PLL). Through Clarke and Park transformations, three-

© 2026 The Authors. This is an open access article distributed under the terms of the Creative Commons Attribution License 4.0 (https://creativecommons.org/licenses/by/4.0/).

DOI: 10.54254/2755-2721/2025.29116

phase AC voltages and currents are converted into direct components in the rotating coordinate system, forming a dual closed-loop control architecture: The outer loop utilizes a PI regulator to track the DC bus voltage setpoint and generate the d-axis current reference value id∗. The inner loop employs a PI controller to output modulation voltages ud∗, uq∗, which are then transformed into three-phase modulation signals via inverse Park and inverse Clarke transformations. These signals drive the switches through three-level space vector pulse width modulation (SVPWM), with midpoint potential balance maintained by adjusting redundant switching states or injecting zero-sequence voltage.

The current controller is pivotal, as its performance directly dictates the overall efficacy of the TP Vienna rectifier. Under d-q axis control, cross-coupling emerges between d-q axis currents; uncompensated, this impairs independent control between axes, leading to suboptimal system performance. To mitigate such coupling and enhance dynamic response, academia has proposed numerous solutions in recent years.

The Current Feedback Decoupling Control (CFDC) method calculates system-generated coupling voltages based on feedback current and speed for feedforward compensation [3]. This approach, characterized by structural simplicity and strong feasibility, remains susceptible to parameter variations.

Reference [4] also adopts feedforward decoupling to compensate cross-coupling terms in the synchronous rotating frame. Recognizing the method's heavy reliance on controlled plant parameters, they propose an improved scheme replacing fixed-coefficient PI controllers with fuzzy adaptive PI regulators, thereby enhancing dynamic response.

Current decoupling based on Internal Model Control (IMC) has been investigated in [5-7], where coupling compensation between d-q axis subsystems is realized through an internal model framework. While offering superior decoupling performance compared to CFDC under parameter variations, this method involves complex model calculations and retains dependence on controller-plant parameter matching and model accuracy, with decoupling performance degrading under parameter mismatches.

A hybrid decoupling strategy combining IMC and sliding mode control is presented in [8], albeit introducing sliding mode chattering. Reference [9] proposes a dual PI-type decoupling method, which aligns with internal model decoupling under specific conditions and exhibits better parameter robustness than traditional feedforward decoupling but struggles with high-order or time-varying coupling.

Jinhwan Jung and Kwanghee Nam analyzed three decoupling approaches: feedforward, internal model, and dual PI decoupling [10], designing a novel dynamic decoupling scheme integrating traditional PI and dual PI methods. They further proposed a decoupling-preserving overmodulation algorithm to account for the impact of subsequent SVPWM overmodulation on dynamic decoupling.

Reference [11] introduces a deviation decoupling control strategy that leverages the advantages of internal model decoupling but suffers from structural complexity and underdamped oscillation issues. In [12], a current loop decoupling control method based on complex vectors is proposed, merging d-q axis current components into complex numbers via complex modeling and controller design. This simplifies the system's mathematical model in the synchronous rotating frame and implicitly addresses cross-coupling, improving response speed and steady-state current accuracy.

Reference [13] presents an inverse system decoupling control method using neural network online identification, where the inverse system comprises multiple integrators and static neural networks, yielding favorable dynamic and static performance for the decoupled system. To enhance system disturbance rejection, Professor Han Jingqing proposed Active Disturbance Rejection

DOI: 10.54254/2755-2721/2025.29116

Control (ADRC) [14], which attributes all uncertainties of the controlled plant to total disturbance, estimated and compensated via an Extended State Observer (ESO), with minimal reliance on plant model parameters during modeling.

Surveying existing research, the current mainstream decoupling control methods still harbor numerous limitations awaiting critical breakthroughs. On one hand, while CFDC boasts a concise structure, it is sensitive to system parameter variations and exhibits weak anti-disturbance capability; although feedforward decoupling and improved fuzzy adaptive PI schemes have optimized dynamic responses, they fail to fundamentally break free from strong parametric dependence on the controlled plant. IMC and its derivative hybrid strategies, despite enhancing decoupling performance under parameter variations, suffer from high computational complexity in modeling, with decoupling efficacy deeply intertwined with model accuracy and parameter matching; performance degrades markedly in cases of parameter mismatch. Meanwhile, dual PI-type decoupling, though demonstrating superior robustness over traditional feedforward methods under specific conditions, struggles to tackle high-order or time-varying coupling scenarios.

On the other hand, complex vector decoupling and inverse system methods, despite optimizing decoupling effects in certain dimensions, are plagued by respective drawbacks: the former relies on intricate complex-domain modeling, while the latter is constrained by the real-time performance and stability of neural network online identification. Even though the ADRC framework achieves estimation and compensation of total disturbances via ESO, the T-LESO employed in LADRC still leaves room for improvement in disturbance observation accuracy and dynamic response speed. Particularly in scenarios involving abrupt changes or mismatches of inductance parameters, its capability to suppress coupling disturbances remains insufficient, making complete decoupling elusive.

To address the aforementioned research bottlenecks, this paper proposes a current decoupling control method based on LADRC improved by DDC-LESO, building upon existing decoupling control theories. This method replaces the T-LESO in traditional LADRC with DDC-LESO, retaining the fundamental architecture of T-LESO while introducing a disturbance differential term as an additional state variable, thereby significantly enhancing the observation accuracy of total system disturbances. This improvement enables the method to transcend the strong inductance parameter dependence of traditional decoupling strategies, achieving complete d-q axis current decoupling even when inductance parameters of the TP Vienna rectifier are mismatched, while simultaneously balancing dynamic response speed and robustness. Through comparative experiments with traditional decoupling methods under inductance parameter variation scenarios, this paper verifies the superiority of the proposed method in parameter robustness and decoupling performance, thus providing a technical pathway for the efficient and stable operation of TP Vienna rectifiers in DC charging systems.

2. Traditional current decoupling method

2.1. Mathematical model of TP Vienna rectifier

In the d-q coordinate system, the mathematical model of the current loop of the TP Vienna rectifier can be expressed in the following form:

DOI: 10.54254/2755-2721/2025.29116

$$\begin{cases} L\frac{di_d}{dt} = e_d - Ri_d + \omega Li_q - U_d \\ L\frac{di_q}{dt} = e_q - Ri_q + \omega Li_d - U_q \end{cases} \begin{cases} L\frac{di_d}{dt} = e_d - Ri_d + \omega Li_q - U_d \\ L\frac{di_q}{dt} = e_q - Ri_q + \omega Li_d - U_q \end{cases} \tag{1}$$

L--The equivalent total inductance of each phase in the AC side of the rectifier, R--The equivalent total resistance value of each phase in the AC side of the rectifier, e_d , e_q —Corresponding values of the three-phase AC voltage in the synchronous rotating dq coordinate system, i_d , i_q —Corresponding values of the three-phase AC in the synchronous rotating dq coordinate system, ω —The angular frequency of the grid voltage, U_d , U_q —denoting the corresponding voltage value between point n in the TP Vienna rectifier topology and the neutral point O of the three-phase AC voltage within the synchronous rotating d-q coordinate system.

Applying the Laplace transform of Equation (1) yields the following equation:

$$\begin{cases} U_d(s) = -Ri_d(s) - sLi_d(s) + \omega Li_q(s) + e_d \\ U_q(s) = -Ri_q(s) - sLi_q(s) - \omega Li_d(s) + e_q \end{cases} \tag{2}$$

As evidenced by Equation (2), a cross-coupling term exists between the d-axis and q-axis. Should the cross-coupled dq-axis currents remain uncompensated, independent control cannot be achieved, thereby degrading the system's control performance.When the D-axis current is adjusted, the coupling term will generate reverse disturbance through the Q-axis current, forming inter-axis interference, resulting in a decline in the ability to track the reference value. The control block diagram when the traditional PI control is adopted, considering the coupling case but it is not decoupled, is shown in Fig. 1, where $K_p = \widehat{L}\omega_c$, $K_i = \widehat{R}\omega_c$

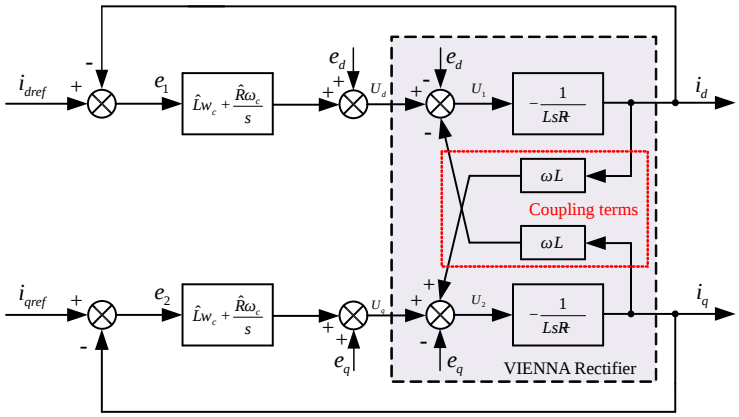


Figure 1. Block diagram of conventional PI control for the current loop of the TP Vienna rectifier when the coupling case is considered without decoupling

2.2. Current feedback decoupling control method for TP Vienna rectifier

To address the issue of cross-coupling terms between the d-axis and q-axis, scholars have proposed the CFDC method, wherein the coupling potentials $i_d\omega\widehat{L}$, $i_q\omega\widehat{L}$ are incorporated into the output of

DOI: 10.54254/2755-2721/2025.29116

the PI controller to mitigate the influence of coupling potentials, thereby achieving decoupling of the rectifier. The control block diagram of CFDC is depicted in Fig. 2. Notably, $\widehat{L}$ represents the estimated reference value of the inductance employed in the controller. In the actual control system of the rectifier, the change of the rectifier resistance has little influence on the decoupling control, so $\widehat{R}=R$ can be used, and the estimated reference value of the inductance will deviate from the actual inductance value of the rectifier during operation.

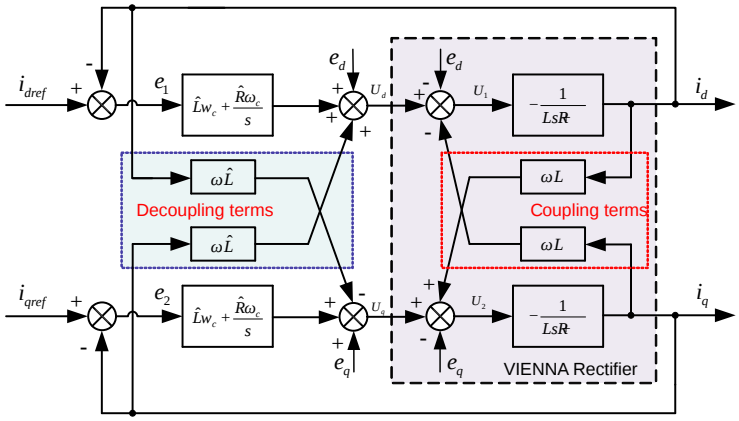


Figure 2. Control block diagram of the CFDC method

The derivation of the closed-loop transfer function of the control model shown in Fig. 2 is as follows.

According to Fig. 2, the current expression of the rectifier dq two-axis output is as follows

$$\begin{bmatrix} i_d \\ i_q \end{bmatrix} = \begin{bmatrix} -\frac{1}{Ls+R} & 0 \\ 0 & -\frac{1}{Ls+R} \end{bmatrix} \begin{bmatrix} U_1 \\ U_2 \end{bmatrix} \tag{3}$$

After derivation, the expression of U_1, U_2 can be obtained as follows:

$$\begin{bmatrix} U_1 \\ U_2 \end{bmatrix} = \begin{bmatrix} \frac{\widehat{L}\omega_c s+\widehat{R}\omega_c}{s} & 0 \\ 0 & \frac{\widehat{L}\omega_c s+\widehat{R}\omega_c}{s} \end{bmatrix} \begin{bmatrix} i_{dref} \\ i_{qref} \end{bmatrix} - \begin{bmatrix} \frac{\widehat{L}\omega_c s+\widehat{R}\omega_c}{s} & \omega\left(L-\widehat{L}\right) \\ \omega\left(\widehat{L}-L\right) & \frac{\widehat{L}\omega_c s+\widehat{R}\omega_c}{s} \end{bmatrix} \begin{bmatrix} i_d \\ i_q \end{bmatrix} \tag{4}$$

Substituting Equation (4) into Equation (3), the closed-loop transfer function expression of the system can be obtained as follows.

$$\begin{bmatrix} i_d \\ i_q \end{bmatrix} = \frac{1}{\Delta_1} \begin{bmatrix} g_{11} g_{12} \\ g_{21} g_{22} \end{bmatrix} \begin{bmatrix} i_{dref} \\ i_{qref} \end{bmatrix} \tag{5}$$

DOI: 10.54254/2755-2721/2025.29116

where $\Delta_1 = G_{11} + G_{22} + G_{11}G_{22} - G_{12}G_{21} + 1$, $g_{11} = G_{11}(1 + G_{22})$, $g_{12} = -G_{12}G_{22}$, $g_{21} = -G_{21}G_{11}$, $g_{22} = G_{22}(1 + G_{11})$, $G_{11} = G_{22} = -\frac{\hat{L}\omega_c s + \hat{R}\omega_c}{(Ls+R)s}$, $G_{12} = -\frac{\omega(L-\hat{L})}{Ls+R}$, $G_{21} = \frac{\omega(L-\hat{L})}{Ls+R}$.

According to Equation (5), it can be concluded that the closed-loop transfer function of d-axis current coupling term is $\frac{g_{12}}{\Delta_1}$, and the closed-loop transfer function of q-axis current coupling term is $\frac{g_{21}}{\Delta_1}$.

2.3. Current internal mode decoupling control method for Tp Vienna rectifier

The current feedback decoupling rectifier of the TP Vienna rectifier can solve the problem of d-q axis coupling to a certain extent, but this method highly depends on the accurate inductance parameters of the rectifier. When the reference inductance is not consistent with the real inductance, it cannot achieve complete decoupling.

Internal Model control (IMC) is an advanced strategy to design a controller based on the mathematical model of the plant. The key idea of IMC is to achieve error-free tracking of reference inputs and strong robustness to external disturbances by embedding a dynamic model of the controlled system (i.e., the "internal model") inside the controller. The schematic diagram of the IMC is shown in Fig. 3:

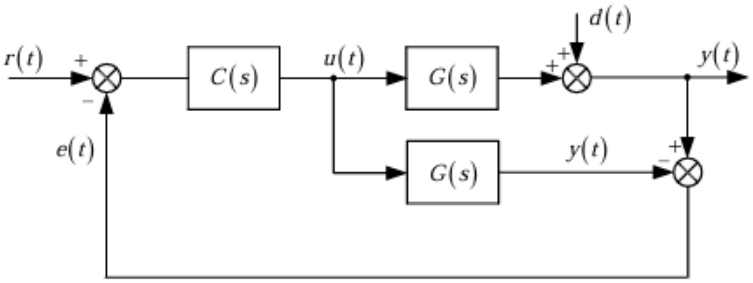


Figure 3. Schematic diagram of IMC

According to Fig. 3, when $\hat{G}(s) \neq G(s)$, there is a discrepancy between the actual model of the control object and the reference model, in this case, the deviation can also be adjusted by the feedback link. When it is applied to the current decoupling control, the deviation can also be adjusted by the feedback link when the reference inductance is not consistent with the real inductance. According to the analysis of IMC, the control block diagram of IMC is shown in Fig. 4:

DOI: 10.54254/2755-2721/2025.29116

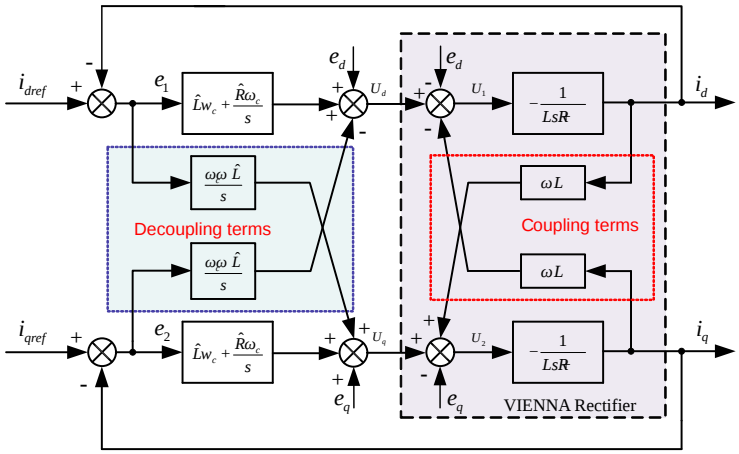


Figure 4. Control block diagram of the IMC

The closed-loop transfer function of the IMC control model shown in Fig. 4 is derived as follows.

Fig. 4 shows that the expression of the relationship between rectifier current error and system control quantity input when ed, eq is ignored is as follows:

$$\begin{bmatrix} U_d \\ U_q \end{bmatrix} = \omega_c \begin{bmatrix} \frac{\hat{L}s+\hat{R}}{s} & \frac{-\omega\hat{L}}{s} \\ \frac{\omega\hat{L}}{s} & \frac{\hat{L}s+\hat{R}}{s} \end{bmatrix} \begin{bmatrix} e_1 \\ e_2 \end{bmatrix} \tag{6}$$

The expression of the relationship between id, iq and Ud, Uq is given below

$$\begin{bmatrix} i_d \\ i_q \end{bmatrix} = \frac{1}{\Delta} \begin{bmatrix} -(Ls+R) & -\omega L \\ \omega L & -(Ls+R) \end{bmatrix} \begin{bmatrix} U_d \\ U_q \end{bmatrix} \tag{7}$$

The closed-loop transfer function expression of the system can be obtained by substituting Equation (6) into Equation (7) as follows.

$$\begin{bmatrix} i_d \\ i_q \end{bmatrix} = \frac{1}{\Delta_2} \begin{bmatrix} g_{11} & g_{12} \\ g_{21} & g_{22} \end{bmatrix} \begin{bmatrix} i_{dref} \\ i_{qref} \end{bmatrix} \tag{8}$$

where $\Delta_2 = \Delta\left(G_{11}+G_{22}+\Delta\right)+G_{11}G_{22}-G_{12}G_{21}$, $g_{11} = G_{11}\left(\Delta+G_{22}\right)-G_{12}G_{21}$, $g_{22} = G_{22}\left(\Delta+G_{11}\right)-G_{12}G_{21}$, $g_{12} = G_{12}\Delta$, $g_{21} = G_{21}$, $G_{11} = G_{22} = -\omega_c\left(\frac{(Ls+R)\left(\hat{L}s+R\right)}{s}+\frac{\omega^2 L\hat{L}}{s}\right)$, $G_{21} = \omega_c\left(\frac{\omega L\left(\hat{L}s+R\right)}{s}-\frac{\omega\hat{L}(Ls+R)}{s}\right)$, $G_{12} = \omega_c\left(\frac{\omega\hat{L}(Ls+R)}{s}-\frac{\omega L\left(\hat{L}s+R\right)}{s}\right)$

DOI: 10.54254/2755-2721/2025.29116

3. Current decoupling control method based on LADRC modified by DDC-LESO

In order to achieve a good decoupling effect, the key is the calculation of the disturbance compensation term. In the previous methods, the disturbance calculation depends on the rectifier model, and the parameter robustness is poor. In addition, the coupling and disturbance for the modeling part are not considered. In order to further improve the decoupling performance of the system, the improved LADRC based on DDC-LESO is applied to the current decoupling control, and good control effect is achieved.

3.1. Traditional second-order ESO(T-LESO)

For a first-order system, consider the transformation of the control plant into the form of a first-order differential equation, which can be expressed as

$$\dot{y} = bu + f(y, \omega, t) \tag{9}$$

Select the state variables $x_1 = y$, $x_2 = f$, $h = \dot{f}$, and write the plant in the form of a state space equation as follows:

$$\begin{cases} \dot{x} = Ax + Bu + Eh \\ y = Cx + Du \end{cases} \tag{10}$$

where $A = \begin{bmatrix} 0 & 1 \\ 0 & 0 \end{bmatrix}$, $B = \begin{bmatrix} b_0 \\ 0 \end{bmatrix}$, $C = [1 \quad 0]$, $D = [0]$, $E = \begin{bmatrix} 0 \\ 1 \end{bmatrix}$, b_0 is an estimate of the parameter b.

Accordingly, a second-order linear state observer is designed

$$\begin{cases} \dot{z}_1 = z_2 - \beta_1 (z_1 - x_1) + b_0 u \\ \dot{z}_2 = -\beta_2 (z_1 - x_1) \end{cases} \tag{11}$$

where, z_1 is the observed value of the state variable x_1; z_2 is the observed value of the state variable x_2; h_1, h_2 is the gain coefficient of the second-order linear state observer. In order to ensure the convergence of the observer, $\beta_1 = 2\omega_0$, $\beta_2 = {\omega_0}^2$ can be obtained from the bandwidth method.

If e_1, e_2 is the error observed by the observer z_1, z_2, respectively, the error expressions obtained from Equations (9), (10) and (11) are described as follows:

$$\begin{cases} e_1 = x_1 - z_1 \\ e_2 = x_2 - z_2 \end{cases} \tag{12}$$

DOI: 10.54254/2755-2721/2025.29116

$$\begin{cases} \dot{e}_1 = e_2 - 2\omega_0 e_1 \\ \dot{e}_2 = \dot{f} - {\omega_0}^2 e_1 \end{cases} \tag{13}$$

By combining Equations (9), (10), (11) and (13), the transfer function $\Phi_{Cz2}(s)$ of the traditional second-order ESO based on perturbed observations and the transfer function $\Phi_{Ce2}(s)$ of the perturbation estimation error can be described as follows:

$$\Phi_{Ce2}(s) = \frac{s^2 + 2\omega_0 s}{(s+\omega_0)^2} \tag{14}$$

$$\Phi_{Cz2}(s) = \frac{{\omega_0}^2}{(s+\omega_0)^2} \tag{15}$$

3.2. Perturbation Differential Compensated Linear Extended State Observer (DDC-LESO)

When the observer observes the disturbance, all the disturbance quantities must be accurately observed in order to achieve complete decoupling of the current loop, because the disturbance forms in the current loop are various and complex. The traditional T-LESO has a heavy burden on interference estimation and cannot observe all interference quantities quickly and accurately. Based on ESO, the disturbance Differential compensated linear extended state Observer (DDC-LESO) adds the disturbance difference observation, which enhances the disturbance observation ability of ADRC.

For the first-order system shown in Equation (9), the state variable $x_1 = y$, $x_2 = f$, $x_3 = \dot{f}$, $h = \ddot{f}$, is selected to write the controlled plant in the form of a state space equation as follows:

$$\begin{cases} \dot{x} = Ax + Bu + Eh \\ y = Cx + Du \end{cases} \tag{16}$$

where $A = \begin{bmatrix} 0 & 1 & 0 \\ 0 & 0 & 1 \\ 0 & 0 & 0 \end{bmatrix}$, $B = \begin{bmatrix} b_0 \\ 0 \\ 0 \end{bmatrix}$, $C = \begin{bmatrix} 1 & 0 & 0 \end{bmatrix}$, $D = [0]$, $E = \begin{bmatrix} 0 \\ 0 \\ 1 \end{bmatrix}$.

Accordingly, DDC-LESO is designed,

$$\begin{cases} \dot{z}_1 = z_2 - \beta_1 (z_1 - x_1) + b_0 u \\ \dot{z}_2 = z_3 - \beta_2 (z_1 - x_1) \\ \dot{z}_3 = -\beta_3 (z_1 - x_1) \end{cases} \tag{17}$$

DOI: 10.54254/2755-2721/2025.29116

where, z_1 is the observed value of the state variable x_1; z_2 is the observed value of the state variable x_3; z_3 is the observed value of the state variable x_3; b_0 is an estimate of the parameter b; h_1, h_2, h_3 are the gain coefficients of DDC-LESO. In order to ensure the convergence of the observer, it can be obtained from the bandwidth method that $\beta_1 = 3\omega_0$, $\beta_2 = 3{\omega_0}^2$, $\beta_3 = {\omega_0}^3$.

If e_1, e_2, e_3 is the error observed by the observer z_1, z_2, z_3, respectively, the error expressions obtained from Equations (9), (16) and (17) are described as follows:

$$\begin{cases} e_1 = x_1 - z_1 \\ e_2 = x_2 - z_2 \\ e_3 = x_3 - z_3 \end{cases} \tag{18}$$

$$\begin{cases} \dot{e}_1 = e_2 - 3\omega_0 e_1 \\ \dot{e}_2 = e_3 - 3{\omega_0}^2 e_1 \\ \dot{e}_3 = \ddot{f} - {\omega_0}^3 e_1 \end{cases} \tag{19}$$

By combining Equations (9), (16), (17) and (19), the traditional second-order ESO transfer function $\Phi_{DDCz2}(s)$ based on the perturbation observations and the transfer function $\Phi_{DDCe2}(s)$ of the perturbation estimation error can be described as follows:

$$\Phi_{DDCe2}(s) = \frac{s^3 + 3\omega_0 s^2}{(s+\omega_0)^3} \tag{20}$$

$$\Phi_{DDCz2}(s) = \frac{3{\omega_0}^2 s + {\omega_0}^3}{(s+\omega_0)^3} \tag{21}$$

According to Equations (14), (15), (20) and (21), the transfer functions of T-LESO and DDC-LESO based on perturbed observations and perturbed observation errors depend only on ω_0. Therefore, when ω_0 is taken to be the same value, the Bode plots of T-LESO and DDC-LESO based on the perturbed observation value and the perturbed observation error can be obtained, as shown in Fig. 5.

DOI: 10.54254/2755-2721/2025.29116

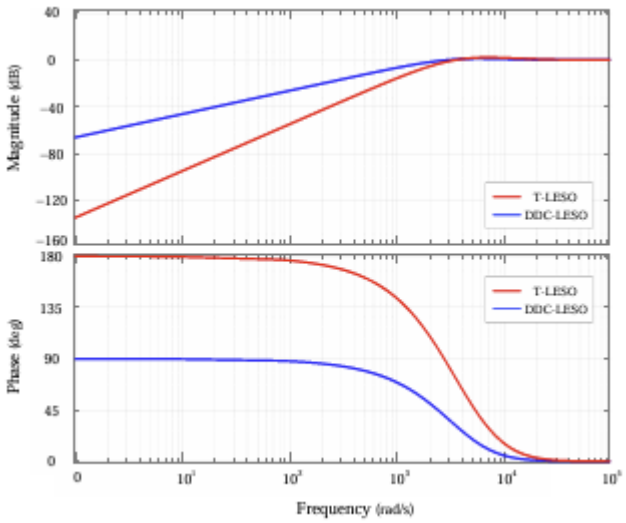


Figure 5. Bode plots of disturbance observation values and observation errors for T-LESO and DDC-LESO under identical parameter settings

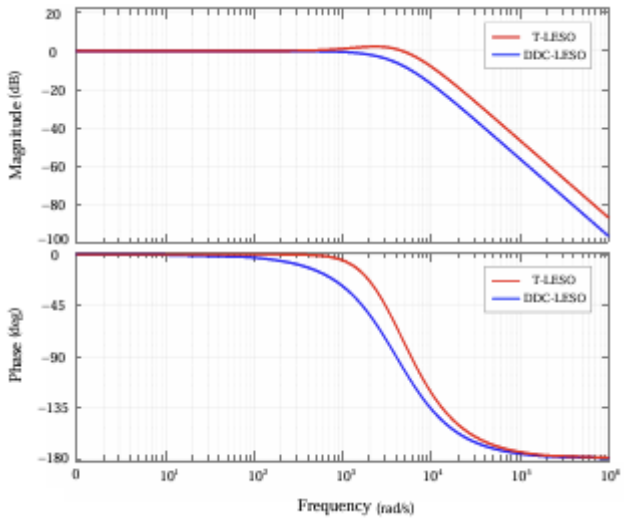


Figure 6. Bode plots of disturbance observation values and observation errors for T-LESO and DDC-LESO under identical parameter settings (higher frequency range)

As illustrated in Fig. 6, under the same condition of parameter ω_0, the DDC-LESO demonstrates a broader scope of disturbance estimation in comparison with the T-LESO. This characteristic not only enhances the system's anti-disturbance performance but also mitigates the high-frequency oscillations that would otherwise be induced by an increase in ω_0.

Notably, in Fig. 5, when parameter ω_0 remains identical, the amplitude gain of the observation error of DDC-LESO with respect to disturbances within the low-frequency range is smaller than that of T-LESO. This further validates that the DDC-LESO exhibits superior disturbance rejection capability relative to the T-LESO.

Based on Equation (1), the first-order equation of state can be constructed as follows:

DOI: 10.54254/2755-2721/2025.29116

$$\begin{cases} \dot{i}_d = -\frac{1}{L}U_d - \frac{R}{L}i_d + \frac{e_d+\omega L i_q}{L} + f_{do} \\ \dot{i}_q = -\frac{1}{L}U_q - \frac{R}{L}i_q + \frac{e_q-\omega L i_d}{L} + f_{qo} \end{cases} \tag{22}$$

The internal and external disturbance of the system is defined as the total disturbance.

$$\begin{cases} f_d = -\frac{R}{L}i_d + \frac{e_d+\omega L i_q}{L} + f_{do} \\ f_q = -\frac{R}{L}i_q + \frac{e_q-\omega L i_d}{L} + f_{qo} \end{cases} \tag{23}$$

According to Equation (22), the disturbance forms in the current loop are complex and diverse. To realize the complete decoupling of the current loop, all disturbance quantities need to be accurately observed. The traditional ESO bears inherent limitations in disturbance estimation, as it struggles to achieve rapid and accurate observation of all disturbance components due to its constrained estimation capacity. To address this deficiency, the DDC-LESO incorporates enhanced observation of the disturbance differential term by building upon the traditional ESO framework, thereby strengthening the disturbance observation capability of the ADRC. The d-q axis current i_d and i_q are defined as the state variable x_1, the total disturbance f_d, f_q is defined as the state variable x_2, and the differential term of disturbance f_d, f_q is extended to the new state variable x_3. The third-order state equation in the form shown in Equation (16) is established, where b_0 is the system control quantity gain $-\frac{1}{L_0}$. The DDC-LESO of the form shown in Equation (17) is constructed, and this observer is used to replace the traditional second-order linear observer. Fig. 7 shows the block diagram of the LADRC structure based on DDC-LESO improvement for the q axis.

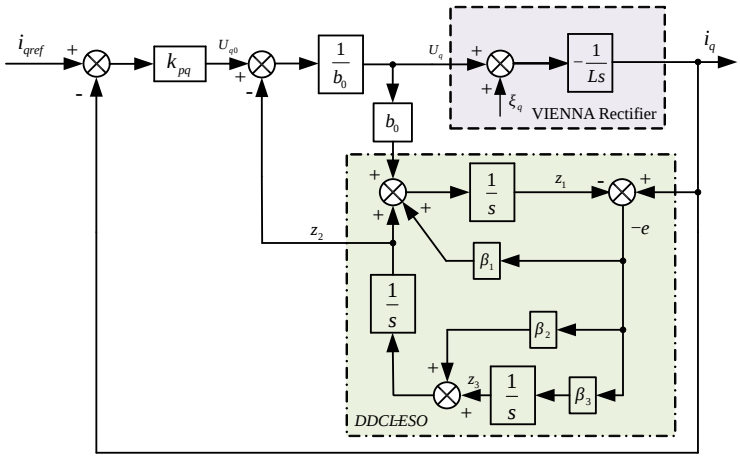


Figure 7. Block diagram of LADRC structure based on DDC-LESO improvement in q axis

3.3. Current decoupling control method based on LADRC modified by DDC-LESO

After obtaining the estimated total disturbance value, disturbance compensation is required. This part is called the state Error feedback (SEF). It provides error feedback between the actual d-q axis current value and the reference value. The initial d-q axis voltage reference values U_{d0}, U_{q0} are obtained by SEF calculation. Where K_p is the controller gain coefficient. z_2 is compensated into

DOI: 10.54254/2755-2721/2025.29116

the initial voltage command value U_{d0}, U_{q0} to obtain the reference voltage reference value U_d, U_q.

$$U_d = \frac{U_{d0} - z_2}{b_0} \tag{24}$$

$$U_q = \frac{U_{q0} - z_2}{b_0} \tag{25}$$

After compensating the disturbance, Equation (1) can be expressed as follows:

$$\begin{cases} i_d = -\frac{1}{Ls}(U_d + \xi_d) \\ i_q = -\frac{1}{Ls}(U_q + \xi_q) \end{cases} \tag{26}$$

where $\xi_d = -Lf_d$, $\xi_q = -Lf_q$.

Finally, the TP Vienna rectifier can be reduced to a first-order pure integration process. At this point, the d-q axis becomes two independent links, and decoupling control can be achieved. DDC-LESO can estimate the total disturbance more accurately by making multiple observations of the disturbance and its differential term. Fig. 8 illustrates the equivalent model of the TP Vienna rectifier, while Fig. 9 presents the block diagram of the current decoupling control for the LADRC incorporating DDC-LESO-based improvements.

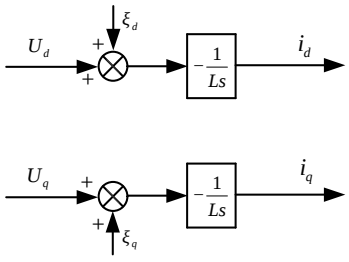


Figure 8. Block diagram of the equivalent model of the TP Vienna rectifier

DOI: 10.54254/2755-2721/2025.29116

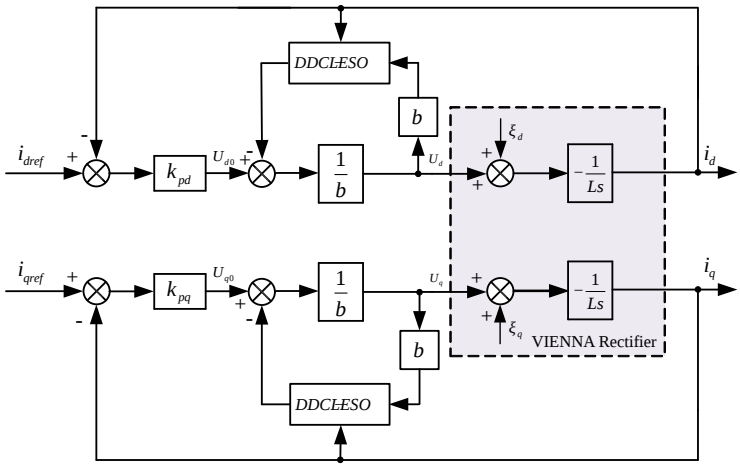


Figure 9. Block diagram of LADRC method based on DDC-LESO modification

By setting $x_1 = y$ in Equation (17) and transforming it into the form of frequency domain as shown below, it can be obtained that:

$$\begin{cases} Z_1(s) = \frac{{\omega_0}^3 + 3{\omega_0}^2 s + 3\omega_0 s^2}{(s+\omega_0)^3} Y(s) + \frac{b_0 s^2}{(s+\omega_0)^3} U(s) \\ Z_2(s) = C(1-A)Y(s) - BCU(s) \\ Z_3(s) = \frac{{\omega_0}^3 s^2}{(s+\omega_0)^3} Y(s) - \frac{b_0 {\omega_0}^3 s}{(s+\omega_0)^3} U(s) \end{cases} \tag{27}$$

where $A = \frac{{\omega_0}^3 + 3{\omega_0}^2 s + 3\omega_0 s^2}{(s+\omega_0)^3}$, $B = \frac{b_0 s^2}{(s+\omega_0)^3}$, $C = \frac{3{\omega_0}^2 s + {\omega_0}^3}{s^2}$.

For the convenience of control, let the controller gain coefficient $K_p = \omega_c$ in the block diagram of Fig. 5, the relationship between the system input U , the system output Y (that is, the actual current value of d-q axis) and the d-q axis current reference value R can be obtained that:

$$U(s) = \frac{1}{b_0}\left[\omega_c (R(s) - Y(s)) - Z_2\right] \tag{28}$$

The system output expression can be obtained from (28), (27) and (9):

$$Y(s) = \frac{1}{D} F(s) + \frac{b_0 \omega_c}{D(b_0 - CB)} R(s) \tag{29}$$

where $D = \frac{s(b_0 - CB) + b_0(\omega_c + C(1-A))}{b_0 - CB}$.

In Equation (29), only considering the relationship between output and coupled disturbance, the transfer function of output and disturbance can be obtained as

DOI: 10.54254/2755-2721/2025.29116

$$Y(s)=\frac{b_0-CB}{s(b_0-CB)+b_0(\omega_c+C(1-A))}F(s) \tag{30}$$

4. Influence of inductance variation on d-q axis current decoupling control

Among the parameters of the rectifier, the d-q axis inductance stands as the most critical one pertaining to current decoupling control. As such, any discrepancy between the actual d-q axis inductance and its pre-estimated value is bound to exert a significant impact on the operational performance of the current control system. This part will compare and analyze the robustness of CFDC, IMC and LADRC control based on DDC-LESO improvement when inductance parameters change.

The CFDC coupling phase transfer functions are $\frac{g_{12}}{\Delta_1}$, $\frac{g_{21}}{\Delta_1}$,

IMC coupled phase transfer functions are $\frac{g_{12}}{\Delta_2}$, $\frac{g_{21}}{\Delta_2}$,

The improved LADRC control coupling phase transfer function based on DDC-LESO is shown in Equation (30).

According to the above expressions, the sensitivity of CFDC, IMC and improved LADRC control based on DDC-LESO to changes in inductance parameters is analyzed. The test is carried out under inductance parameters of $400\mu H$, resistance of $60mR$, capacitance of $800\mu F$, and bandwidth of current control system of $1000Hz$.

For the realization of unity power factor control, the q-axis current of the TP Vienna rectifier must be regulated to zero. In the analysis of the rectifier's current decoupling effect, the d-axis current is typically varied by adjusting the DC-side load, with the q-axis current decoupling effect being observed amid such variations. The subsequent analysis will focus on the robustness of the q-axis current control against changes in inductor parameters.

Fig. 10, Fig. 11, Fig. 12. The three figures are Bode diagrams of the current coupled phase transfer function in the q-axis of the three decoupling modes in time.

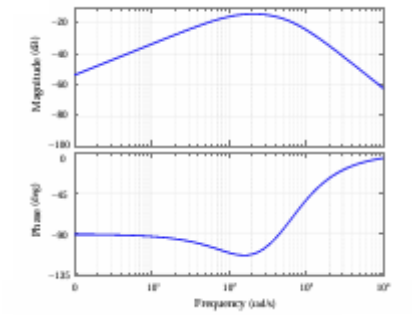


Figure 10. Bode plot of the current-coupled phase transfer function in the q-axis of the CFDC

DOI: 10.54254/2755-2721/2025.29116

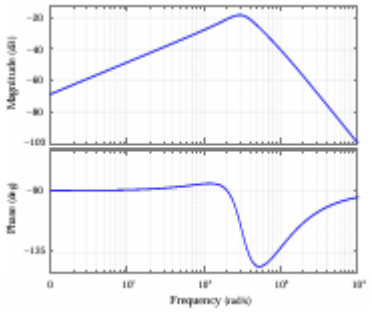


Figure 11. Bode plot of the current-coupled phase transfer function in the Q-axis of the IMC

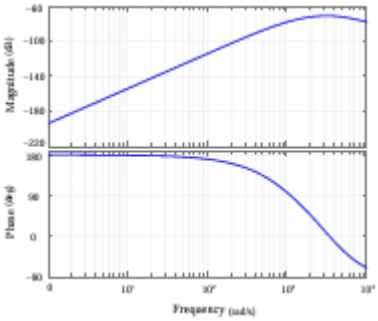


Figure 12. Bode of LADRC decoupled Q-axis current-coupled phase transfer function based on DDC-LESO modification

Fig. 10 shows the Bode plot of the CFDC coupling coefficient when $\widehat{L} = 2L$. The controller bandwidth chosen here is 1000. When $\widehat{L} = 2L$, the coupling gain of the CFDC in the low frequency band is -50dB. This indicates that there is a large amount of current coupling and complete decoupling of the current loop cannot be achieved. Fig.11 illustrates the Baud plot of the IMC coupling coefficient when $\widehat{L} = 2L$. The controller bandwidth chosen here is 1000. When $\widehat{L} = 2L$, the coupling gain of IMC is lower than that of CFDC, indicating that the decoupling effect is improved. But the degree of improvement is not obvious. Fig.12 illustrates the Bode plot of the LADRC decoupled q-axis current coupled phase transfer function based on DDC-LESO modification when $\widehat{L} = 2L$. The controller bandwidth chosen here is 1000. When $\widehat{L} = 2L$, the coupling gain of LADRC improved by DDC-LESO is lower than that of CFDC and IMC, which indicates that the decoupling effect is improved significantly.

Fig. 13, Fig. 14, and Fig. 15. The three figures are Bode plots of the q-axis current coupled phase transfer function when $\widehat{L} = 0.5L$ for the three decoupling modes.

DOI: 10.54254/2755-2721/2025.29116

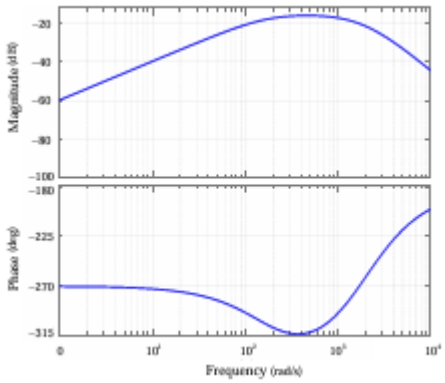


Figure 13. Bode plot of the current-coupled phase transfer function in the q-axis of the CFDC

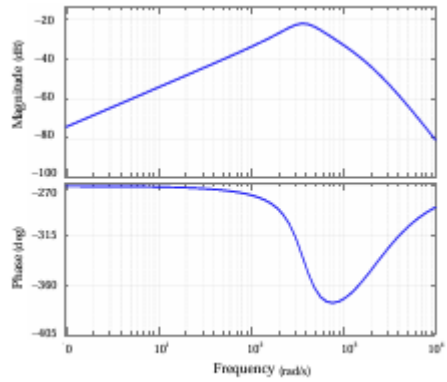


Figure 14. Bode plot of the current-coupled phase transfer function in the Q-axis of the IMC

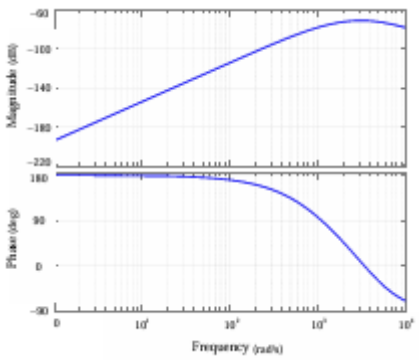


Figure 15. Bode plot of LADRC decoupled Q-axis current-coupled phase transfer function based on DDC-LESO modification

Fig. 13 shows the Bode plot of the CFDC coupling coefficient when $\widehat{L} = 0.5L$. The controller bandwidth chosen here is 1000. When $\widehat{L} = 0.5L$, the coupling gain of the CFDC in the low frequency band is -50dB. This indicates that there is a large amount of current coupling and complete decoupling of the current loop cannot be achieved. Fig. 14 illustrates the Baud plot of the IMC coupling coefficient when $\widehat{L} = 0.5L$. The controller bandwidth chosen here is 1000. When

DOI: 10.54254/2755-2721/2025.29116

$\widehat{L} = 0.5L$, the coupling gain of IMC is lower than that of CFDC, indicating that the decoupling effect is improved. But the degree of improvement is not obvious. Fig. 15 illustrates the Bode plot of the LADRC decoupled q-axis current coupled phase transfer function based on DDC-LESO modification when $\widehat{L} = 0.5L$. The controller bandwidth chosen here is 1000. When $\widehat{L} = 0.5L$, the coupling gain of LADRC improved by DDC-LESO is lower than that of CFDC and IMC, which indicates that the decoupling effect is improved significantly.

5. Simulation analysis

To evaluate the robustness of the proposed current decoupling method with respect to inductor parameter mismatches, under the operating condition where the d-axis current of the TP Vienna rectifier is maintained at 20.5A, the DC side load is increased from 0.387Ω to 0.508Ω , which will lead to a step response of the D-axis current, and the change of id at this time is recorded.

Fig. 16, Fig. 17 and Fig. 18 presents the experimental results under $\widehat{L} = 2L$ using the three methods. Fig. 16 indicates that when $\widehat{L} = 2L$, the overshoot of the q-axis current is 0.95A and the settling time is 0.11s using CFDC when the d-axis current is mutated. Fig. 17 shows that when $\widehat{L} = 2L$, the overshoot of the q-axis current is 0.19 A and the settling time is 0.07s using IMC when the d-axis current is mutated. Fig. 18 shows that when $\widehat{L} = 2L$, the q-axis current is able to achieve complete decoupling using the LADRC decoupling based on the DDC-LESO improvement when the d-axis current is abrupt. LADRC decoupling based on DDC-LESO modification is the most robust.

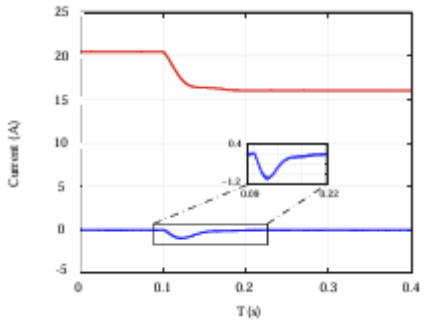


Figure 16. Current waveform diagram of CFDC when$\widehat{L} = 2L$

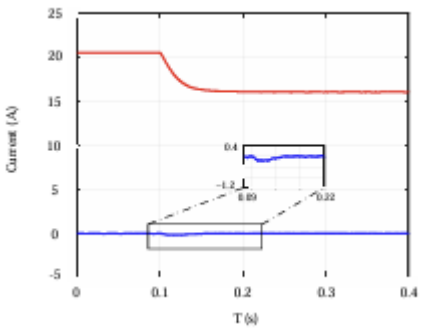


Figure 17. Current waveform diagram of the IMC when$\widehat{L} = 2L$

DOI: 10.54254/2755-2721/2025.29116

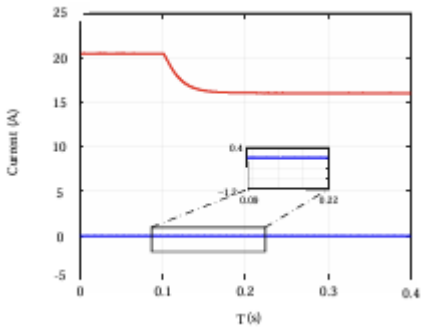


Figure 18. Current waveform diagram of LADRC decoupling control based on improved DDC-LESO when$\widehat{L} = 2L$

Fig. 19, Fig. 20 and Fig. 21 presents the experimental results under $\widehat{L} = 0.5L$ using the three methods. Fig. 16 indicates that when $\widehat{L} = 0.5L$, the overshoot of the q-axis current is 0.48A and the settling time is 0.11s using CFDC when the d-axis current is mutated. Fig. 17 shows that when $\widehat{L} = 0.5L$ occurs, when the D-axis current undergoes a sudden change, using IMC, the overshoot of the Q-axis current is 0.3A and the stabilization time is 0.08s. Fig. 18 shows that when $\widehat{L} = 0.5L$, the q-axis current is able to achieve complete decoupling using the LADRC decoupling based on the DDC-LESO improvement when the d-axis current is abrupt. LADRC decoupling based on DDC-LESO modification is the most robust.

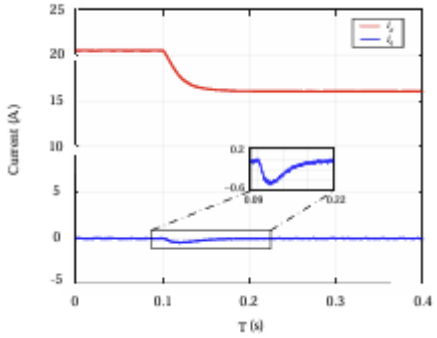


Figure 19. Current waveform diagram of CFDC when$\widehat{L} = 0.5L$

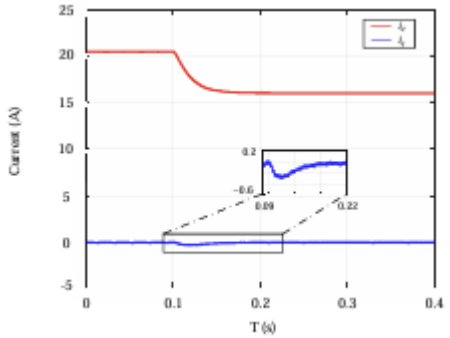


Figure 20. Current waveform diagram of the IMC when$\widehat{L} = 0.5L$

DOI: 10.54254/2755-2721/2025.29116

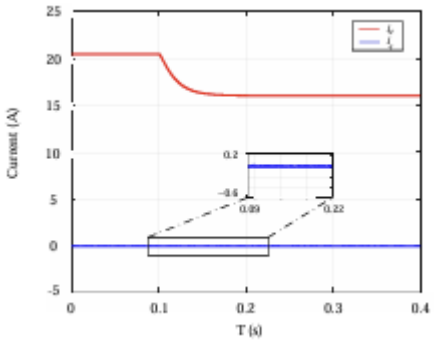


Figure 21. Current waveform diagram of LADRC decoupling control based on improved DDC-LESO when$\widehat{L} = 0.5L$

6. Conclusion

In this paper, an improved LADRC current decoupling control method based on DDC-LESO is proposed. The proposed method exhibits excellent decoupling performance and strong robustness. Through in-depth theoretical derivation, comparative analysis of transfer functions, and systematic simulation verification, the following conclusions are drawn:

(1) Traditional current decoupling methods have inherent limitations in dealing with inductance parameter mismatches, failing to achieve complete decoupling under parameter variations.

Specifically, the CFDC relies heavily on accurate inductance parameter estimation. Its decoupling effect is directly determined by the matching degree between the estimated inductance and the actual inductance. When parameter mismatches occur, the cross-coupling terms between the d-q axes cannot be effectively compensated, resulting in significant residual coupling currents. This leads to impaired independent control between axes and degraded system performance.

The IMC improves decoupling performance compared to CFDC by embedding the system model into the controller, but it still depends on the accuracy of the model parameters. When inductance parameters change, its decoupling effect is suppressed, and it cannot fundamentally eliminate the impact of parameter mismatches, making it difficult to meet the requirements of high-performance current control.

(2) The DDC-LESO, as the core innovation of the proposed method, significantly enhances the disturbance observation capability compared to the traditional T-LESO.

By introducing the disturbance differential term as an additional state variable on the basis of T-LESO, DDC-LESO expands the dimension of state observation, enabling more comprehensive and accurate capture of the total system disturbances. Theoretical analysis of transfer functions and Bode diagram comparisons show that under the same parameter settings, DDC-LESO has a wider disturbance estimation bandwidth and a smaller low-frequency observation error gain. This improvement not only strengthens the real-time performance of disturbance observation but also avoids high-frequency oscillations caused by excessive observer bandwidth, laying a solid foundation for precise disturbance compensation.

(3) The improved LADRC based on DDC-LESO realizes complete decoupling of d-q axis currents, independent of inductance parameter matching.

By integrating DDC-LESO into the LADRC framework, the proposed method estimates and compensates for total disturbances in real time. After compensation, the dynamic model of the TP Vienna rectifier is simplified to a first-order pure integration process, and the d-q axes are transformed into two independent control links, fundamentally eliminating cross-coupling between

DOI: 10.54254/2755-2721/2025.29116

axes. Simulation results verify that whether the inductance parameter is doubled or halved, the q-axis current remains stable at the set value when the d-axis current undergoes a step change, achieving complete decoupling. This indicates that the method breaks free from the dependence on inductance parameters, which is a key breakthrough compared to traditional methods.

(4) The proposed method comprehensively improves the dynamic response speed and parameter robustness of the system.

In terms of dynamic performance, when the d-axis current has a step change due to load variations, the q-axis current controlled by the improved LADRC shows no overshoot and has a faster settling time, which is significantly better than CFDC.

In terms of parameter robustness, the transfer function analysis of the coupling phase shows that the proposed method maintains a lower coupling gain in both low and high frequency bands under inductance parameter variations, and its anti-disturbance capability against parameter mismatches is significantly stronger than that of traditional methods. This ensures the stable operation of the TP Vienna rectifier under complex working conditions such as inductance drift caused by temperature changes or magnetic saturation.

(5) The proposed method provides a reliable technical solution for high-performance operation of TP Vienna rectifiers in DC charging systems.

Given the unique advantages of the TP Vienna rectifier in DC charging scenarios, the improved LADRC based on DDC-LESO effectively solves the bottleneck of current decoupling control under parameter variations. It ensures efficient AC/DC conversion with unity power factor, stable DC bus voltage, and strong anti-interference capability, laying a technical foundation for the safe, efficient, and stable operation of DC charging systems.

References

[1] Kolar, J.W., Friedli, T. (2013). The Essence of Three-Phase PFC Rectifier Systems—Part I. IEEE Transactions on Power Electronics, , 28(1): 176-198.
[2] Friedli, T., Hartmann, M., Kolar, J.W. The Essence of Three-Phase PFC Rectifier Systems—Part II. IEEE Transactions on Power Electronics, 2014, 29(2): 543-560.
[3] Morimoto, S., Sanada, M., Takeda, Y. Wide-speed operation of interior permanent magnet synchronous motors with high performance current regulator. IEEE Transactions on Industry Applications, 1994, 30(4): 920 – 926.
[4] Li, F., Li, Z., Zhang, X., Guo, Y. Robust Model Predictive Current Control With Adaptive Extended-State-Observer for Permanent Magnet Synchronous Motor. 2023 IEEE International Conference on Predictive Control of Electrical Drives and Power Electronics (PRECEDE), Wuhan, China, 2023.
[5] Harnefors, L., Nee, H.P. Model-based current control of AC machines using the internal model control method. IEEE Transactions on Industry Applications, 2002, 34(1): 133-141.
[6] Bi, P. “Decoupling Current Control for AC Induction Machine.” Jilin University, MA thesis. 2023.
[7] Yang, Y. Optimization of Field Oriented Control for Permanent Magnet Synchronous Motor in Electric Vehicle Based on Torque-Speed-Current MAP. Jilin University, MA thesis. 2018.
[8] Zhou, H., Wen, X., Zhao, F. Zhang, J. Decoupled current control of permanent magnet synchronous motors drives with sliding mode control strategy based on internal model. Proceedings of the Chinese Society of Electrical Engineering, vol. 32. no. 15, pp. 91–99, May. 2012.
[9] Jung, J., Lim, S., Nam, K. PI type decoupling control scheme for high speed operation of induction motors [C]. IEEE Power Electronics Specialists Conference. IEEE, 1997.
[10] Jung, J., Nam, K. A dynamic decoupling control scheme for high-speed operation of induction motors . IEEE Transactions on Industrial Electronics, 1999, 46(1): 100-110.
[11] Zhou, Z. A induction motor decouple conrol method. Proceedings of the CSEE, vol. 23, no. 2, pp. 121-125, 2003.
[12] Zhang, J., Bu, F., Xu, Z., Sun, P. (2024). Flux-Weakening Control of IPMSM Based on Complex Vector Decoupling. 2024 IEEE 7th International Electrical and Energy Conference (CIEEC), Harbin, China, , pp. 4176-4181.

DOI: 10.54254/2755-2721/2025.29116

[13] Jiang, C., Zhu, H., Wang, X. (2023). Decoupling Control of Outer Rotor Coreless Bearingless Permanent Magnet Synchronous Generator Based on Fuzzy Neural Network Inverse System. IEEE Transactions on Transportation Electrification, 9(3), 3908-3917.
[14] Han, J.Q. (2009). From PID to active disturbance rejection control. IEEE Trans. Ind. Electron., vol. 56(3), 900-906.
[15] Cui, Y., Yin, Z., Luo, P., Yuan, D., Liu, J. (2024). Linear Active Disturbance Rejection Control of IPMSM Based on Quasi-Proportional Resonance and Disturbance Differential Compensation Linear Extended State Observer, " in IEEE Transactions on Industrial Electronics, 71(10), 11910-11924.